

A directly observable, Zeeman-insensitive nuclear spin coherence in solution

James Eills,^{1,2} Anushka Singh,¹ Amir Mahyar Teimoori,^{3,4} Irene Marco Rius,² Morgan W. Mitchell,^{3,5} and Michael C. D. Tayler^{3, a)}

¹⁾*Institute of Biological Information Processing, Structural Biochemistry (IBI-7), Forschungszentrum Jülich, 52428 Jülich, Germany*

²⁾*IBEC – Institute for Bioengineering of Catalonia, 08028 Barcelona, Spain.*

³⁾*ICFO – Institut de Ciències Fotòniques, The Barcelona Institute of Science and Technology, 08860 Castelldefels (Barcelona), Spain.*

⁴⁾*Department of Electrical and Computer Engineering, Isfahan University of Technology, 84153-83111 Isfahan, Iran.*

⁵⁾*ICREA – Institució Catalana de Recerca i Estudis Avançats, 08010 Barcelona, Spain.*

(Dated: 13 January 2026)

ABSTRACT

Clock transitions are well known in atomic and solid-state systems, but are largely unexplored in molecular liquids. Here we demonstrate a clock-like, nuclear-spin avoided crossing in $[1-^{13}\text{C}]$ -fumarate that supports long-lived and directly observable coherences at ultralow magnetic field: a three-spin transition $|S_0\alpha\rangle \leftrightarrow |T_{+1}\beta\rangle$ near 400 nT exhibits a shallow crossing with a frequency minimum of ~ 2 Hz. The transition is first-order immune to magnetic field perturbations and displays a lifetime of 25 s, around three times the longest single-spin T_2^* . Sensitivity to effective pseudo-fields is also demonstrated, including the internal dipolar field of the sample.

I. INTRODUCTION

Spin-resonance spectroscopy techniques including nuclear magnetic resonance (NMR) and electron paramagnetic resonance (EPR) traditionally involve detecting single-quantum transitions between Zeeman states, at frequencies that vary linearly with magnetic field. Achieving high spectral resolution therefore depends critically on maintaining homogeneous fields, essential for both precision measurements¹ and extracting signals from noisy or crowded spectra. This is often challenging in inhomogeneous environments, particularly in porous materials and other structures with strong magnetic susceptibility variations².

There are, however, several established methods to curb loss of resolution caused by magnetic inhomogeneity. One is by selective detection from only a small fraction of the sample's volume³, using space-selective excitation; the field variation decreases together with the effective linear dimension of the sample. Alternatively, homonuclear zero-quantum NMR⁴⁻⁸ anti-diagonal COSY⁹ and other two-dimensional spectroscopy procedures use dark

transitions with zero frequency-vs.-field derivative to circumvent the limitation. These recover high-resolution spectra in systems where conventional methods fail, but come at a cost: lower signal strength, plus the time cost of indirect point-by-point sampling.

In this paper we investigate another scenario: coherence detection at avoided level crossings. Two energy states of a quantized system will always exhibit an avoided crossing (a.k.a., level anticrossing or LAC) when they have the same symmetry and are mutually coupled by an interaction that is noncommuting with a dominant tunable Hamiltonian term.¹⁰ The mutual coupling maintains a minimum energy separation between the states that keeps them from intersecting at fields where they would otherwise have equal energy. In our case, the tuning Hamiltonian term is the Zeeman interaction between spins and an external magnetic field \mathbf{B} , and the noncommuting terms that are spin-spin J -couplings. The crossing field $|\mathbf{B}| = B_{\text{LAC}}$ is defined by $df/d|\mathbf{B}|_{B_{\text{LAC}}} = 0$, which means that the transition frequency f is first-order immune to spectral broadening caused by field inhomogeneity, or ‘zero first-order Zeeman’ (ZEFOZ).

One system that demonstrates ZEFOZ transitions in the solution state is the molecule $[1-^{13}\text{C}]$ -fumarate, which comprises three scalar-coupled nuclear spins (two ^1H , one ^{13}C , both with quantum number $I = 1/2$, see Fig. 1) giving a LAC in the sub-earth’s-field region, c. 400 nT. This crossing is exploited in parahydrogen-induced hyperpolarization (PHIP)¹¹, a technique that can produce fumarate in a near-pure spin state for metabolite imaging in vitro¹², and in vivo^{13,14}. Adiabatic passage through the LAC is exploited to convert parahydrogen singlet order to observable magnetization¹⁵. In further support of the choice of this molecule to study ZEFOZ transitions, the homogeneous relaxation of spins in fumarate is slow, approaching a 1 minute lifetime for the singlet state^{16,17} due to a lack of other spin-active nuclei, and weak internuclear dipolar couplings.

We first review the theory of the ZEFOZ transition in fumarate, from its coherent evolution to homogeneous and inhomogeneous relaxation, and detection in real time with sensitive magnetometry¹⁸. We then report experimental measurements of the frequency (2–5 Hz) and de-

^{a)}Electronic mail: michael.tayler@icfo.eu

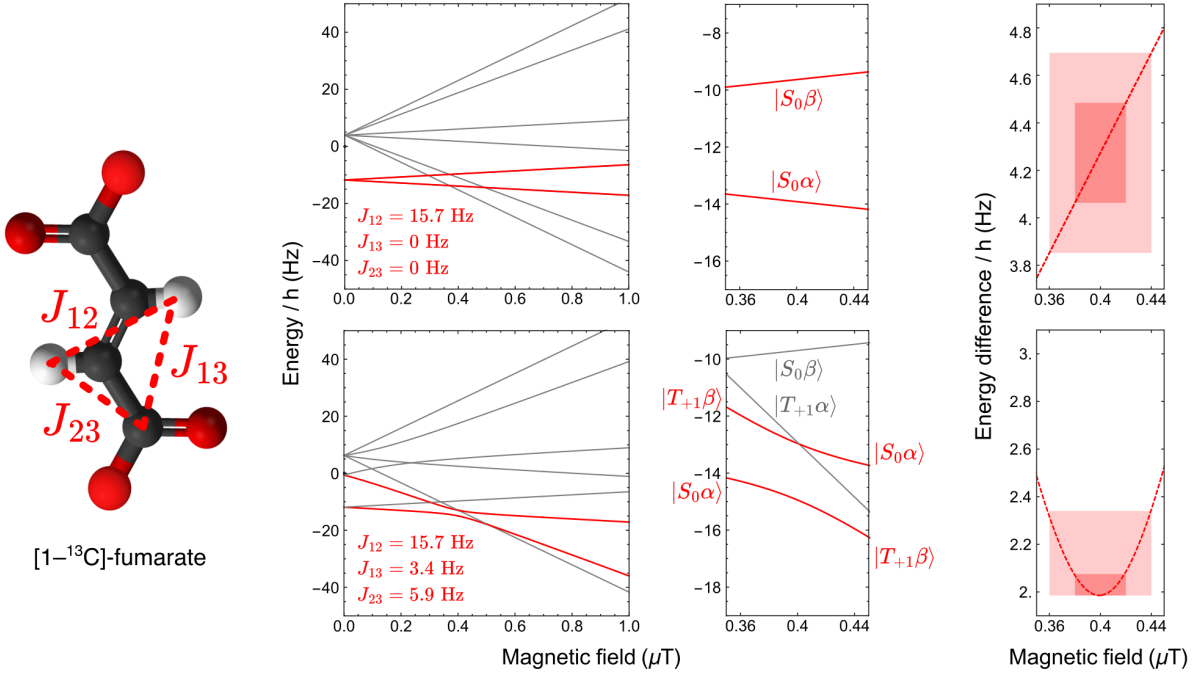


FIG. 1. Energy levels of $[1-^{13}\text{C}]\text{-fumarate}$ in magnetic fields below $1\text{ }\mu\text{T}$. Upper plots correspond to the fictional scenario of non-coupled ^1H and ^{13}C spins, with $J_{13} = J_{23} = 0\text{ Hz}$. Lower plots represent the actual scenario using experimentally measured heteronuclear J-couplings, as listed. The expansion shows that across a field range of c. 100 nT the LAC transition is much less sensitive to spectral broadening; shaded rectangles in the lower plot have a lower aspect ratio $\Delta E : \Delta B_z$.

decay time of the coherence (up to 26 s) following PHIP-polarization, and excitation by nonadiabatic field switching. Notably, the coherence lifetime at $|\mathbf{B}| = B_{\text{LAC}}$ outlasts the slowest conventional T_2^* by a factor of around 3. Nonlinear dynamics are also observed, attributed to back-actions of the system's own magnetization. These are discussed in relation both to nuclear spin hyperpolarization and exotic physics detection.

II. THEORY OF THE ULTRALOW-FIELD LAC IN $[1-^{13}\text{C}]\text{-FUMARATE}$

The nuclear spin Hilbert space of $[1-^{13}\text{C}]\text{-fumarate}$ is eight dimensional ($[2I+1]^3 = 8$), though since the total projection angular momentum (m_I) is a conserved quantum number, the space exhibits a disconnected structure, comprising non-interacting subspaces of relatively low dimension 1,3,3 and 1 for $m_I = -3/2, -1/2, +1/2$ and $+3/2$, respectively. The subspaces with dimension ≥ 2 ($m_I = \pm 1/2$) support avoided crossings, and we will focus on the one with $m_I = +1/2$, which couples a predominantly ^1H singlet-like state (in the Zeeman-product notation $|\alpha\beta\alpha\rangle \equiv |\alpha_{\text{H}_1}\rangle \otimes |\beta_{\text{H}_2}\rangle \otimes |\alpha_{\text{C}}\rangle$)

$$|\phi_a\rangle = |S_0\alpha\rangle \equiv (|\alpha\beta\alpha\rangle - |\beta\alpha\alpha\rangle)\sqrt{2} \quad (1)$$

to two triplet-like states

$$|\phi_b\rangle = |T_{+1}\beta\rangle \equiv |\alpha\alpha\beta\rangle, \quad (2\text{a})$$

$$|\phi_c\rangle = |T_0\alpha\rangle \equiv (|\alpha\beta\alpha\rangle + |\beta\alpha\alpha\rangle)\sqrt{2}. \quad (2\text{b})$$

It is under positive B_z that field-insensitive behavior occurs. The $m_I = -1/2$ counterpart subspace (comprising mixtures of $|S_0\beta\rangle$, $|T_{-1}\alpha\rangle \equiv |\beta\beta\alpha\rangle$ and $|T_0\beta\rangle$) behaves identically to $m_I = +1/2$ for a reversed sign of \mathbf{B} .

A. Static properties

The nuclear-spin Hamiltonian of the molecule in solution, in units of \hbar , is

$$H = \sum_{j=1}^3 \left[-\gamma_j B_z I_{jz} + 2\pi \sum_{k < j} J_{jk} \mathbf{I}_j \cdot \mathbf{I}_k \right], \quad (3)$$

where γ_j are the gyromagnetic ratios, J_{jk} are scalar spin-spin coupling in units of Hz, and I_{jz} are the Cartesian spin operators. In the basis $\{|\phi_a\rangle, |\phi_b\rangle, |\phi_c\rangle\}$, the matrix representation of H shows states are connected by the respective sum and difference of the heteronuclear pair couplings, $J_{\Sigma} = J_{13} + J_{23}$ and $J_{\Delta} = J_{13} - J_{23}$:

$$H_{B_z} \sim \begin{bmatrix} -3J_{12} & -J_{\Delta}\sqrt{2} & J_{\Delta} \\ -J_{\Delta}\sqrt{2} & J_{12} - J_{\Sigma} & J_{\Sigma}\sqrt{2} \\ J_{\Delta} & J_{\Sigma}\sqrt{2} & J_{12} \end{bmatrix} \left(\frac{\pi}{2}\right) - \begin{bmatrix} \gamma_3 & 0 & 0 \\ 0 & \gamma_1 + \gamma_2 - \gamma_3 & 0 \\ 0 & 0 & \gamma_3 \end{bmatrix} \left(\frac{B_z}{2}\right). \quad (4)$$

This representation illustrates a conventional NMR regime, where at large fields (in practice above a few μT) the basis states are eigenstates of H . Only the couplings on the diagonal, J_{12} and J_Σ , are detectable energy differences.

The LAC, in contrast, occurs outside the high-field regime and can be approximated by:

$$B_{\text{LAC}} \approx \text{sign}(m) \frac{\pi(4J_{12} - J_{13} - J_{23})}{2(\gamma_1 - \gamma_3)}. \quad (5)$$

At B_{LAC} , $\langle \phi_a | H | \phi_a \rangle$ and $\langle \phi_b | H | \phi_b \rangle$ are equal, and H_{B_z} becomes:

$$H_{B_{\text{LAC}}} \sim - \begin{bmatrix} 1 & 0 & 0 \\ 0 & 1 & 0 \\ 0 & 0 & 1 \end{bmatrix} \frac{\gamma_{\text{H}} B_{\text{LAC}}}{2} \quad (6)$$

$$+ \begin{bmatrix} -2J_{12} - J_\Sigma & -2\sqrt{2}J_\Delta & \cdot \\ -2\sqrt{2}J_\Delta & -2J_{12} - J_\Sigma & \cdot \\ \cdot & \cdot & 6J_{12} - J_\Sigma \end{bmatrix} \left(\frac{\pi}{4}\right).$$

The known J-coupling values in aqueous solution, $J_{12} = 15.70 \text{ Hz}$, $J_{13} = 5.94 \text{ Hz}$ and $J_{23} = 3.40 \text{ Hz}$, predict this field to lie near $+400 \text{ nT}$.^{19,20} The elements marked “.” are negligible at leading order due to $|J_{12}| \gg |J_\Sigma|$ and $|J_{12}| \gg |J_\Delta|$. The result is a set of eigenstates that are well approximated as a 2-level subspace; the symmetric and antisymmetric combinations of $|\phi_a\rangle$ and $|\phi_b\rangle$, plus the near-isolated state $|\phi_c\rangle$. The ab separation depends principally on the coupling difference,

$$\omega_{\text{LAC}} = \pi\sqrt{2}|J_\Delta|, \quad (7)$$

or $J_\Delta/\sqrt{2}$ in Hz. A second-order-corrected frequency that accounts for the non-secular elements is $\omega_{\text{LAC}} = \pi\sqrt{2}(1 - x + x^2)|J_\Delta|$ where $x = J_\Sigma/(4J_{12})$.

From Eq. 6 we see the microscopic origin of a field-insensitive point: the Zeeman portion of the Hamiltonian is proportional to the unit operator, which ensures that ω_{LAC} is stationary to first order in $B_z - B_{\text{LAC}}$. This can be tested via a perturbative expansion around B_{LAC} , which yields the quadratic dependence

$$\omega_{\text{LAC}}(\delta B) = \omega_{\text{LAC}}(0) + \frac{(\gamma_{\text{H}} - \gamma_{\text{C}})^2 \delta B^2}{2\pi\sqrt{2} J_\Delta} + O(\delta B^4) \quad (8)$$

For small offset fields $\delta B = (B_z - B_{\text{LAC}}) \ll |\omega_{\text{LAC}}/\gamma_{\text{H}}|$. Eq. 8 is plotted in the right panel of Fig. 1.

Now comparing the first derivative in δB ,

$$\frac{d\omega_{\text{LAC}}}{dB_z}|_{B_{\text{LAC}}} = \frac{(\gamma_{\text{H}} - \gamma_{\text{C}})^2}{\pi\sqrt{2} J_\Delta} \delta B, \quad (9)$$

with that of a single-quantum (SQ) transition in the high-field, weak-coupling regime,

$$|d\omega_{\text{SQ}}/dB_z| \geq \gamma_{\text{C}}, \quad (10)$$

we may estimate the range of δB for which the LAC transition is less sensitive to inhomogeneous broadening. This range roughly equates to a ^1H Larmor frequency offset smaller than J_Δ , or between 350 nT and 450 nT as illustrated by the shaded rectangles in Fig. 1.

B. Dynamic properties

The dynamics of the near-isolated states $|\phi_a\rangle$ and $|\phi_b\rangle$ are conveniently described within an effective operator subspace $\mathcal{S}^{(ab)} = \{E, A_x, A_y, A_z\}$, where we define

$$\begin{aligned} E &= |\phi_a\rangle\langle\phi_a| + |\phi_b\rangle\langle\phi_b|, \\ A_x &= (|\phi_a\rangle\langle\phi_b| + |\phi_b\rangle\langle\phi_a|)/2, \\ A_y &= i(|\phi_a\rangle\langle\phi_b| - |\phi_b\rangle\langle\phi_a|)/2, \\ A_z &= (|\phi_a\rangle\langle\phi_a| - |\phi_b\rangle\langle\phi_b|)/2, \end{aligned} \quad (11)$$

to satisfy $[E, A_\xi] = 0$ and $[A_j, A_k] = i\epsilon_{jkl}A_l$. The commutation relations ensure the unitary time-evolution of the spin density operator ρ in $\mathcal{S}^{(ab)}$ is equivalent to a precession or 3D-rotation (R) of the 3-vector projection

$$\rho^{(ab)}(t) = [(A_x|\rho(t)), (A_y|\rho(t)), (A_z|\rho(t))], \quad (12)$$

about the angular velocity vector

$$\begin{aligned} \omega_{\text{LAC}} &= \left(\frac{(A_x|H)}{(A_x|A_x)}, \frac{(A_y|H)}{(A_y|A_y)}, \frac{(A_z|H)}{(A_z|A_z)} \right) \\ &= ((\gamma_{\text{H}} - \gamma_{\text{C}})\delta B, 0, \pi\sqrt{2}J_\Delta); \end{aligned} \quad (13)$$

$$\text{i.e., } \rho^{(ab)}(t) \approx R(\omega_{\text{LAC}} t) \rho^{(ab)}(0). \quad (14)$$

At $\delta B = 0$, $\rho^{(ab)}$ thus precesses about the A_x axis, and at large offsets the tends to about the axis $\text{sign}(\delta B)A_z$ (see Fig. 2, top left). We note that the vector norm $|\omega_{\text{LAC}}|$, when expanded as a power series in the limit of small δB , coincides exactly with the expression in Eq. 8 for ω_{LAC} , derived by perturbation theory.

The three-dimensional model accurately reproduces the full system dynamics for representative initial states, $\rho(0)$, including cases involving a sudden, i.e., *nonadiabatic*, switch from a high field to values near B_{LAC} . For example, in the lower part of Fig. 2, using $\rho(0) \propto A_z$, we observe that at fields $B_z > 200 \text{ nT}$ the full-system evolution projected onto $\mathcal{S}^{(ab)}$ exhibits the precession-like motion of Eq. 14. In further support of the validity of the isolated two-level description, the vector norm of $\rho^{(ab)}(t)$ is nearly constant. A small exception, however, is towards zero and negative fields where isolation breaks down due to the second LAC.

The evolution of A_z is closely related to *magnetogenesis* processes that may follow when fumarate and AA'X spin-system analogs are generated via PHIP reactions. Assuming a 100% reaction yield, the initial condition is a pure singlet-polarized spin system, corresponding to $\rho(0) = |S_0\alpha\rangle\langle S_0\alpha| + |S_0\beta\rangle\langle S_0\beta| \equiv 1/4 - \mathbf{I}_1 \cdot \mathbf{I}_2$. The first ($|\phi_a\rangle$) term has a nonzero projection $\rho^{(ab)}(0) = (0, 0, 0.5)$ on $\mathcal{S}^{(ab)}$, while the second is the counterpart in the $m = -1/2$ manifold. It is the difference between the two population terms that gives rise to nuclear magnetization along z , which we find by projecting $\rho(t)$ onto the magnetization operator, $M_\xi = \sum_i \gamma_i I_i \xi$. Given a precession

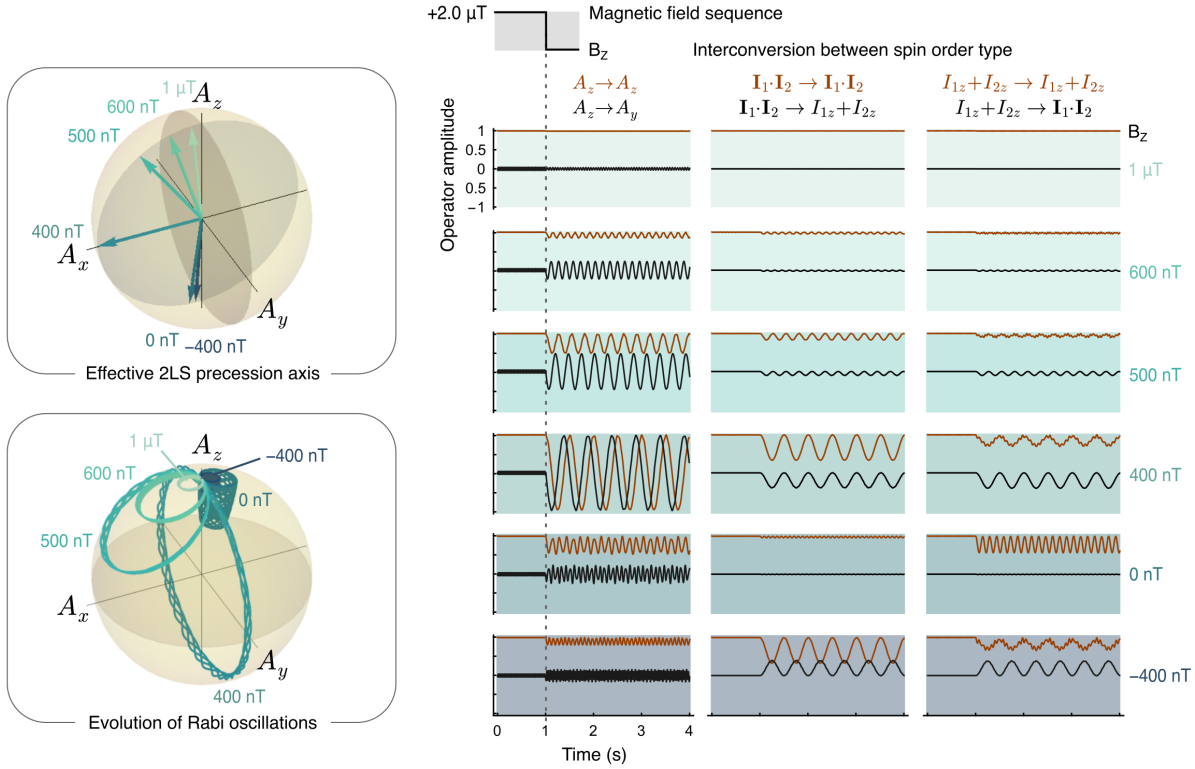


FIG. 2. **Left:** Vector model representation of the $\{|\phi_a\rangle, |\phi_b\rangle\}$ subspace in $[1-^{13}\text{C}]\text{-fumarate}$. Upper sphere indicates the B_z -dependent effective field orientation in the xz plane (Eq. 13) for the combined Zeeman and J-coupling Hamiltonian (Eq. 3). Lower sphere shows simulated time-evolution trajectories of $\rho^{(\text{ab})}(0) = A_z$ under H , which closely reflects precession about the effective axes. **Right:** Simulated operator trajectories when switching from an initial field of $B_z = 2 \mu\text{T}$ to a lower field after 1 s. Plots show the transformation amplitude of the operator on the left side of the arrows (\rightarrow) to those indicated on the right. $I_{1z} + I_{2z}$ is proportional to the total ^1H magnetization along z , and $\mathbf{I}_1 \cdot \mathbf{I}_2$ is the traceless ^1H spin-singlet order. Conversion of A_z is most efficient at $B_z = +B_{\text{LAC}} = +0.4 \mu\text{T}$, reducing as the field offset increases, including $B_z = -B_{\text{LAC}}$, while magnetization-to-singlet and singlet-to-magnetization conversions are effective equally (except opposite in sign) at $B_z = \pm B_{\text{LAC}}$ due to the same initial population of the $m = \pm 1/2$ manifolds. Switching to zero field yields no net magnetization.

angle (θ) between A_z and A_y at $\delta B = 0$, we find

$$\langle M_z \rangle \equiv \left(\left[A_z \cos \theta + \frac{E}{2} + |S_0 \beta\rangle \langle S_0 \beta| \right] |M_z\rangle \right) / 2 \quad (15)$$

$$= \frac{(\gamma_H - \gamma_C)}{4} (\cos \theta - 1), \quad (16)$$

and $\langle M_x \rangle = \langle M_y \rangle = 0$. Thus, magnetization oscillates parallel to B_z between zero and a maximum proportional to $(\gamma_H - \gamma_C)$, and the heteronuclear character of the spin system is crucial to rendering the transition directly observable. We note that free evolution (or $\theta = \omega_{\text{LAC}} t$) contrasts with previous methods of converting from singlet to magnetization order via adiabatic field sweeping procedures, e.g., a field ramp between $-\delta B$ ($\theta = 0$) and $+\delta B$ ($\theta = \pi$).²⁰ In the free evolution case, the conversion efficiency for nonzero δB is narrowband, limited by

$$|\theta| \leq 2 \arctan \left| \frac{\delta B (\gamma_H - \gamma_C)}{\pi \sqrt{2} J_\Delta} \right|. \quad (17)$$

The third column of Fig. 2 indicates the reverse process, conversion to $\mathbf{I}_1 \cdot \mathbf{I}_2$ from M_z , which is a scenario possible when the sample is pre-polarized at high field.

C. Relaxation

Spin-singlet populations and singlet-triplet coherences often outlive conventional relaxation modes because they are partially immune to pair-correlated pathways. In high magnetic fields, for example in $[1-^{13}\text{C}]\text{-fumarate}$ at $\sim 10 \text{ T}$, population difference between the ^1H singlet and triplet manifolds decays with an exponential time constant $T_S = 46 \pm 7 \text{ s}$, substantially longer than $T_1 \sim 23 \text{ s}$ reported for the same system.¹⁷ Other studies report long T_S values in comparable regimes.²¹

It is natural to ask whether such protection persists at the LAC field. A basic analysis suggests that $[1-^{13}\text{C}]\text{-fumarate}$ at the LAC field does *not* support long-lived coherences. The eigenstates $(|\phi_a\rangle \pm |\phi_b\rangle)/\sqrt{2}$ each contain equal mixtures of singlet and triplet components, which eliminates the exchange symmetry that protects against correlated relaxation.²²

A simple random-field model makes this explicit. Let the ^1H spins experience zero-mean stochastic fields \mathbf{B}_1 and \mathbf{B}_2 with root-mean-square amplitude B_{rms} and cross-correlation $c_{12} = \langle \mathbf{B}_1 \cdot \mathbf{B}_2 \rangle / B_{\text{rms}}^2$. In the motional-

narrowing limit, Redfield theory gives the auto-relaxation rates of the reduced subspace operators

$$\frac{1}{T_{A_x}} = \frac{1}{T_{A_y}} = \gamma_H^2 B_{\text{rms}}^2 \tau_c (5 - c_{12})/2, \quad (18)$$

$$\frac{1}{T_{A_z}} = 2\gamma_H^2 B_{\text{rms}}^2 \tau_c. \quad (19)$$

These rates become identical when $c_{12} = 1$. For comparison, an isolated ^{13}C nucleus should relax with

$$\frac{1}{T_2(^{13}\text{C})} = 2\gamma_C^2 B_{\text{rms}}^2 \tau_c, \quad (20)$$

which is much slower due to $(\gamma_C/\gamma_H)^2 \approx 0.06$. Thus, operation at the LAC does not provide protection against homogeneous relaxation, and any advantage instead stems from reduced sensitivity to inhomogeneity in δB (Eq. 9 *vs.* Eq. 10).

III. EXPERIMENTAL RESULTS

We performed a series of experiments where [$1-^{13}\text{C}$]-fumarate was polarized at natural ^{13}C isotopic abundance (2.2% ^{13}C) in an initial state of near-pure ^1H spin-singlet order, following the PHIP procedure described in the Methods section. A precursor molecule, acetylene dicarboxylate, was combined with para- H_2 (5 bar, 115 °C) in the ambient laboratory field to generate the hyperpolarized product in aqueous solution (60 mM in D_2O). After reaction, the solution was rapidly cooled, depressurized, and then transferred into a magnetically shielded solenoid energized to a field strength of $B_z = 2\text{ }\mu\text{T}$. In this location, the longitudinal magnetization was monitored using alkali-vapor magnetometry²⁰. The time dependence of the magnetization was measured following a sudden (sub-ms) switching of B_z to near B_{LAC} , producing signals like those shown by the black curves in the center column of Fig. 2. An illustration of these operations is given in Fig. 3.

A. Frequencies of the LAC transition

The position and shape of B_{LAC} was determined by measuring a series of polarized fumarate samples. In each experiment, the polarized [$1-^{13}\text{C}$]-fumarate was placed inside the magnetic shield and the B_z field was switched to a different value, between 200 nT and 600 nT. This resulted in an oscillating magnetic signal which was measured by the OPM. The fumarate signal frequencies as a function of evolution field B_z are shown in the lower left part of Fig. 3 and the overall shape is in excellent agreement with a parabola in the vicinity of the minimum, around 400 nT, turning linear at offsets above $\sim \pm 100$ nT. Fitting the eigenvalues of H to the data points gives the dashed curve and refined values of the molecular J -couplings $J_{12} = 15.92$ Hz and $J_{\Sigma} = 9.34$ Hz, (which

are mostly pinned down by B_{LAC}), and $J_{\Delta} = 2.514$ Hz (mostly pinned down by ω_{LAC}). The fitted minimum is $B_z = 406(2)$ nT and $\omega_{\text{LAC}}/(2\pi) = 1.995(5)$ Hz.

These values of B_{LAC} and ω_{LAC} are around 20 nT and 0.22 Hz lower, respectively, than the predictions of Eq. 5 and Eq. 7 using the same J -coupling values. The discrepancy arises due to the non-secular Hamiltonian terms that couple $\{|\phi_a\rangle, |\phi_b\rangle\}$ with $|\phi_c\rangle$, but are accounted adequately upon including the $J_{\Sigma}/(4J_{12})$ correction term.

A variant of this experiment was also performed using a single hyperpolarized sample, where B_z was switched to a different value every 2 s to trace out the frequency curve in a one-shot experiment (Fig. 3, lower right). This method also gives an excellent estimation of the LAC field minimum, despite the shorter measurement time at each field point. The 2 s evolution time was chosen to allow for at least a few oscillation periods at all B_z values, for accurate quantification of the signal frequencies. The evolution time affects the overall spin system evolution since the magnetization end-point at each time step is not synchronized, and will therefore affect the signal amplitude for the next time step, but the signal frequencies still match the predicted values.

B. Coherence decay rate

The other defining aspect of the ZEFOZ point is the coherence decay rate. Following a sudden jump to 406 nT, the coherence decayed approximately monoexponentially with a time constant of 25(1) s. This decay was substantially slower than that of the slowest observable oscillation in the non strongly coupled spin system – the ^{13}C single-quantum coherence – for which we measured a transverse relaxation time of $T_2^* = 8.5(5)$ s at $B_z = 2\text{ }\mu\text{T}$. The latter measurement was performed by first magnetizing the PHIP-polarized sample via a 2-s constant-adiabaticity field sweep from $B_z = 50$ nT to $B_z = 2\text{ }\mu\text{T}$, and then applying a Rabi excitation pulse. Even though these measurements were carried out at slightly lower field strength, the comparison with the single-quantum ^{13}C coherence decay demonstrates an exceptionally long lifetime of the LAC coherence.

We also found the decoherence rate in the sudden-switching experiment to be strongly field-dependent within the $|\delta B| < 100$ nT region surrounding the anti-crossing at $B_z = 400$ nT. The rate is a pronounced minimum at B_{LAC} , and increases by close to a factor of 3 at $\delta B = \pm 100$ nT. Outside this region the decay rate was nearly constant, within experimental uncertainty. Such behavior is consistent with inhomogeneous broadening as the dominant dephasing mechanism: away from B_{LAC} , the transition frequency should vary approximately linearly with B_z , so that a fixed field distribution (ΔB) should produce an essentially fixed spread of frequency (Δf) across the sample ($|\Delta B/\Delta f| = |\gamma_H - \gamma_C|/(2\pi)$). This interpretation is supported by Fig. 1, which shows that the transition frequency is indeed in the linear

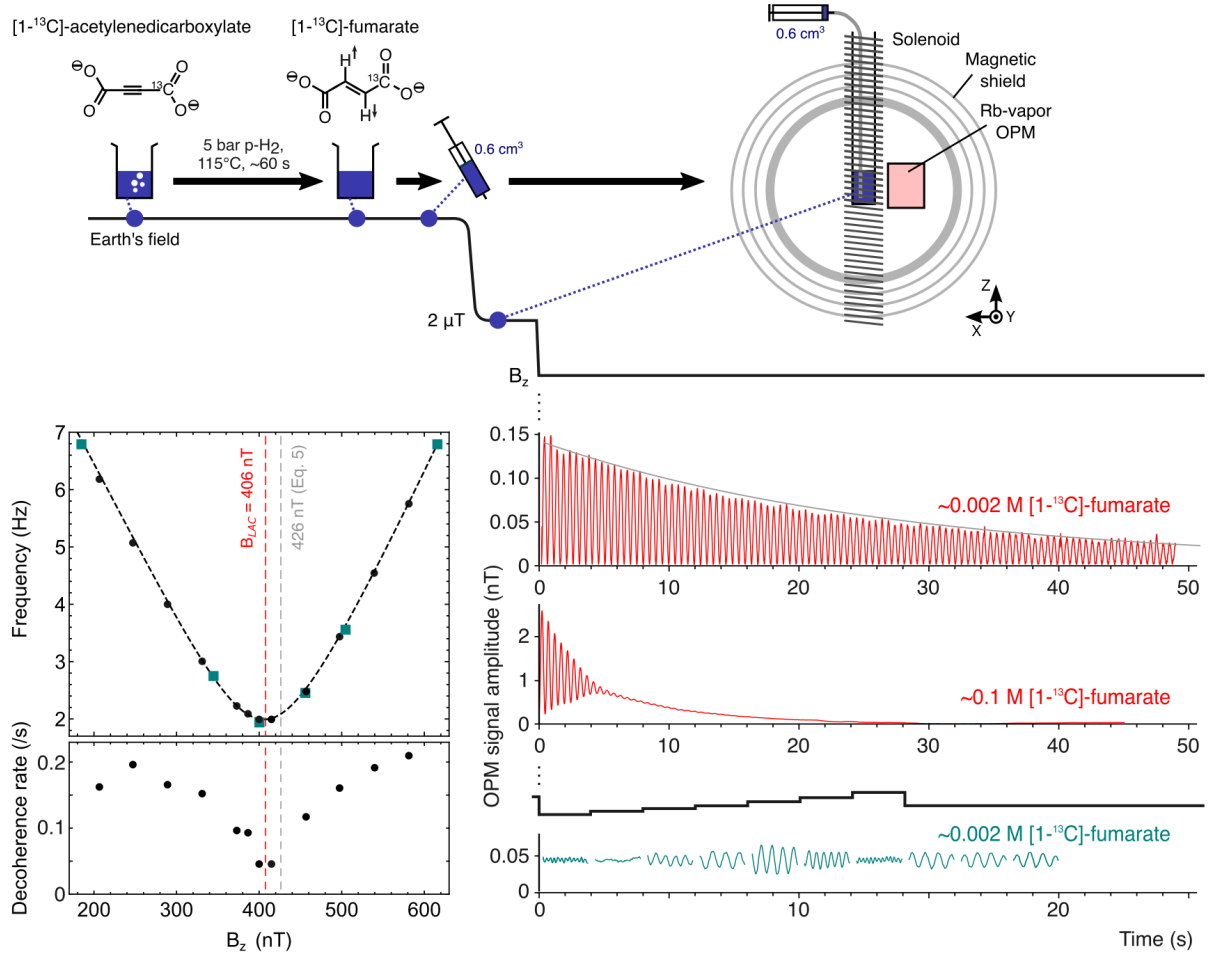


FIG. 3. Solution-state LAC coherences in hyperpolarized $[1-^{13}\text{C}]\text{-fumarate}$ observed via magnetometry. Top: Experimental scheme, showing the initialization of $[1-^{13}\text{C}]\text{-fumarate}$ in a near-pure ^1H -singlet state by reaction of the precursor with para- H_2 , followed by syringe transfer to a low-field setup for subsequent field-switching operations and measurement of the nuclear magnetization using an OPM. Bottom: Experimental results. On the right, magnetization curves from sample experiments are shown. To the left are two plots showing the fitted frequency and decoherence rate at different B_z evolution fields. On the coherence frequency plot, the black dashed curve is the calculated eigenvalue difference between the evolution states of the Hamiltonian in Eq. 4, using best-fit spin-spin coupling parameters $J_{12} = 15.92 \text{ Hz}$, $J_{\Sigma} = 9.34 \text{ Hz}$ and $J_{\Delta} = 2.514 \text{ Hz}$. Dashed red and gray lines indicate the predicted B_{LAC} field from calculating the eigenvalues of the Hamiltonian in Eq. 4, and calculated from Eq. 5, respectively. Curve/data-point colors indicate: (Black) multiple experiments, each with a single switch from $2 \mu\text{T}$ to a chosen evolution field B_z ; (Teal) a single experiment with multiple switches to a different B_z field every 2 s.

regime for $B_z < 300 \text{ nT}$ and for $B_z > 500 \text{ nT}$.

C. High magnetization effects

The sudden-switch experiment to $B_z = 406 \text{ nT}$ was repeated using a precursor that was 99% $[^{13}\text{C}_1]$ enriched, yielding an initial condition of PHIP-polarized $[1-^{13}\text{C}]\text{-fumarate}$ at roughly 45-fold higher concentration than in the natural-abundance sample. In this case, the oscillatory magnetization appeared at the same frequency as in the low-concentration experiment but decayed rapidly (within $\sim 5 \text{ s}$) with a distinctly non-exponential profile. Following disappearance of the oscillatory signal, a non-

oscillating component persisted, which relaxed exponentially on a longer 15–20 s timescale.

The faster decay of the oscillatory signal for the enriched sample is attributed to an inhomogeneity generated by the sample itself. At the much higher ^{13}C concentration, the PHIP-polarized fumarate produces a substantial magnetization, and the associated dipolar (demagnetizing) field,²³ $\mathbf{B}_d(\mathbf{r}) \propto \mathbf{M}(\mathbf{r})$, is no longer negligible across the sample volume. We quantified the self-generated field by magnetizing the sample to its maximum via an adiabatic sweep through the LAC, from $B_z = 0.05 \mu\text{T}$ to $B_z = 2 \mu\text{T}$, then applying a small-tip-angle pulse to create oscillating transverse magnetization in the sample's own field; a measured 2 Hz shift in the ^1H

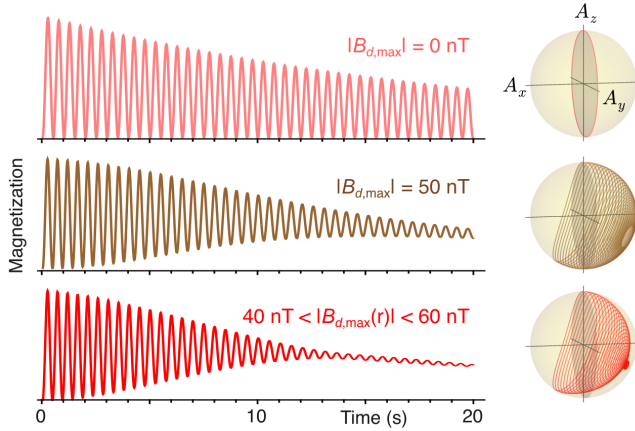


FIG. 4. A model representation of the ‘high magnetization’ regime through simulated trajectories of the $\rho^{(ab)}$ Bloch vector and magnetization projection $\langle M_z(t) \rangle \propto (1 - \langle A_z(t) \rangle)/2$. Each row shows evolution from the same initial condition, $\rho^{(ab)}(0) = A_z$, $\omega_{\text{LAC}}/(2\pi) = 2\text{ Hz}$, for different fields: (top) a constant on-resonance field, $\delta B = 0$; (center) a time-varying pseudo-field due to the macroscopic magnetization $\delta B(t) = B_{d,\text{max}} \times \langle M_z(t) \rangle$, with uniform $B_{d,\text{max}} = 50\text{ nT}$; (bottom) an average of trajectories with time-dependent δB , across a uniform distribution of $B_{d,\text{max}}$ between strengths 40 nT and 60 nT . The latter best replicates the magnetization trajectory for 99%- ^{13}C -enriched [$1-^{13}\text{C}$]-fumarate in Fig. 3.

Larmor frequency corresponds to a mean internal dipolar field of $|B_d| \sim 50\text{ nT}$. Based on Eq. 13, this shift may change the effective field axis substantially, varying between parallel to A_x for the non-magnetized sample at the LAC point and around 40° out of plane at the maximum dipolar field point. A simulated trajectory of $\rho^{(ab)}(t)$ and $M_z(t)$ due to these non-linear, near-resonant dynamics is shown in Fig. 4, where we see the nuclear spin analog of a Josephson oscillation, i.e., self-locking between the magnetization and mean dipolar field axes. Inhomogeneity across the sample volume, which is in practice certain, can further reduce the oscillation time. These effects and possible mitigation strategies (e.g., dipolar field decoupling) may be investigated in more detail in future work.

IV. DISCUSSION AND CONCLUSIONS

The results presented here demonstrate that dilute aqueous solutions of [$1-^{13}\text{C}$]-fumarate support a hyperpolarized coherence with a lifetime of $> 20\text{ s}$ when the magnetic field is tuned precisely to $B_z = B_{\text{LAC}}$. The coherence lifetime exceeds the ^{13}C single-quantum T_2^* by a factor of 3 and shows a pronounced dependence on the detuning from B_{LAC} , δB : the decay rate exhibits a sharp minimum at $B_z = B_{\text{LAC}}$ and increases upon moving away from this point. This behavior is a defining signature of a ZEFOZ transition, and the remaining decoherence time can reflect weaker second-order processes,

including sample-specific effects.

The high robustness of ZEFOZ coherences is frequently exploited in other quantum-mechanical systems to overcome T_2^* limits. For example: Hyperfine anticrossings in atomic clocks; Rare-earth-crystal quantum memories where nuclear-spin lifetimes can reach hours²⁴; NV-diamond magnetometers²⁵; Superconducting *fluxonium* qubits^{26,27} where qubit frequency is a stationary point with respect to junction flux. To our best knowledge, the directly observable ZEFOZ transition in fumarate is the first studied for ^1H and ^{13}C nuclear spins in a molecule.

Another feature of this work is that it reveals high-magnetization back-action effects in an entirely conventional, low-field, ambient-temperature setting. In past studies, strong internal dipolar fields have been accessed only under extreme conditions, e.g., hyperpolarized liquid ^3He or ^{129}Xe , or in ultrahigh magnetic fields. Beyond fundamental interest, these results are directly relevant to the practical uses of PHIP and related techniques that rely on generating exceptionally large nuclear magnetization for metabolic imaging and the polarization of other molecular species. Given that many molecules contain J-coupled networks exhibit LACs in the sub-earth’s field range and can be hyperpolarized²⁸, it is likely that additional ZEFOZ-like transitions and high-magnetization phenomena will be investigated in future. Maleic acid dimethyl ester is one such candidate²⁹ which can be hyperpolarized via a room-temperature PHIP reaction and – because of its high solubility – produce demagnetizing fields at least an order of magnitude higher than those achieved here in fumarate.³⁰

ACKNOWLEDGMENTS

The work described is funded by: the Spanish Ministry of Science MCIN with funding from European Union NextGenerationEU (PRTR-C17.I1) and by Generalitat de Catalunya “Severo Ochoa” Center of Excellence CEX2019-000910-S; the Spanish Ministry of Science projects DHYMOND (PID2024-160223OB-I00), SEE-13-MRI (CPP2022-009771) plus RYC2020-029099-I and RYC2022-035450-I, funded by MCIN/AEI /10.13039/501100011033; Generalitat de Catalunya through the CERCA program; Agència de Gestió d’Ajudts Universitaris i de Recerca Grant Nos. 2017-SGR-1354 and 2021-FILB.01039; Fundació Privada Cellex; Fundació Mir-Puig; and the BIST–“la Caixa” initiative in Chemical Biology (CHEMBIO). The project has received funding from the European Union’s Horizon 2020 Research and Innovation Programme under the Marie Skłodowska-Curie Grant Agreement 101063517. This work was supported by the Initiative and Networking Fund of the Helmholtz Association (Project No. DB002399).

COMPETING INTERESTS

The authors declare no competing interests.

DATA AVAILABILITY

Experimental data files, processing scripts, and simulation codes are publicly accessible via the web at [|Zenodo link to be added on publication|](https://zenodo.org/record/1234567).

REFERENCES

- ¹W. Heil, C. Gemmel, S. Karpuk, Y. Sobolev, K. Tullney, F. Allmendinger, U. Schmidt, M. Burghoff, W. Kilian, S. Knappe-Gräfeberg, A. Schnabel, F. Seifert, and L. Trahms, “Spin Clocks: Probing Fundamental Symmetries in Nature,” *Ann. Phys.* **525**, 539–549 (2013).
- ²M. E. Lacey, R. Subramanian, D. L. Olson, A. G. Webb, and J. V. Sweedler, “High-Resolution NMR Spectroscopy of Sample Volumes from 1 nL to 10 μ L,” *Chem. Rev.* **99**, 3133–3152 (1999).
- ³A. Bax and R. Freeman, “Enhanced NMR Resolution by Restricting the Effective Sample Volume,” *J. Magn. Reson.* (1969) **37**, 177–181 (1980).
- ⁴W. P. Aue, E. Bartholdi, and R. R. Ernst, “Two-dimensional spectroscopy. application to nuclear magnetic resonance,” *J. Chem. Phys.* **64**, 2229–2246 (1976).
- ⁵M. Munowitz and A. Pines, “Multiple-Quantum Nuclear Magnetic Resonance Spectroscopy,” *Science* **233**, 525–531 (1986).
- ⁶S. Vathyam, S. Lee, and W. S. Warren, “Homogeneous NMR Spectra in Inhomogeneous Fields,” *Science* **272**, 92–96 (1996).
- ⁷S. Cai, W. Zhang, and Z. Chen, “High-Resolution Solution NMR Spectra in Inhomogeneous Magnetic Fields,” *Curr. Anal. Chem.* **5**, 70–83 (2009).
- ⁸P. Pelupessy, E. Rennella, and G. Bodenhausen, “High-Resolution NMR in Magnetic Fields with Unknown Spatiotemporal Variations,” *Science* **324**, 1693–1697 (2009).
- ⁹C. Terenzi, A. J. Sederman, M. D. Mantle, and L. F. Gladden, “Enabling High Spectral Resolution of Liquid Mixtures in Porous Media by Antidiagonal Projections of Two-Dimensional ^1H NMR COSY Spectra,” *J. Phys. Chem. Lett.* **10**, 5781–5785 (2019).
- ¹⁰T. Eck, “Level crossings and anticrossings,” *Physica* **33**, 157–162 (1967).
- ¹¹J. Eills, D. Budker, S. Cavagnero, E. Y. Chekmenev, S. J. Elliott, S. Jannin, A. Lesage, J. Matysik, T. Meersmann, T. Prisner, J. A. Reimer, H. Yang, and I. V. Koptyug, “Spin Hyperpolarization in Modern Magnetic Resonance,” *Chem. Rev.* **123**, 1417–1551 (2023).
- ¹²J. Eills, E. Cavallari, C. Carrera, D. Budker, S. Aime, and F. Reineri, “Real-Time Nuclear Magnetic Resonance Detection of Fumarase Activity Using Parahydrogen-Hyperpolarized [$1-^{13}\text{C}_2$]Fumarate,” *J. Am. Chem. Soc.* **141**, 20209–20214 (2019).
- ¹³F. A. Gallagher, M. I. Kettunen, D.-E. Hu, P. R. Jensen, R. i. á. Zandt, M. Karlsson, A. Gisselsson, S. K. Nelson, T. H. Witney, S. E. Bohndiek, G. Hansson, T. Peitersen, M. H. Lerche, and K. M. Brindle, “Production of Hyperpolarized [$1,4-^{13}\text{C}_2$]malate from [$1,4-^{13}\text{C}_2$]fumarate is a Marker of Cell Necrosis and Treatment Response in Tumors,” *Proc. Natl. Acad. Sci. U.S.A.* **106**, 19801–19806 (2009).
- ¹⁴M. Gierse, L. Nagel, M. Keim, S. Lucas, T. Speidel, T. Lohmeyer, G. Winter, F. Josten, S. Karaali, M. Fellermann, J. Scheuer, C. MÄller, F. van Heijster, J. Skinner, J. LÄffler, A. Parker, J. Handwerker, A. Marshall, A. Salhov, B. El-Kassem, C. Vassiliou, J. W. Blanchard, R. Picazo-Frutos, J. Eills, H. Barth, F. Jelezko, V. Rasche, F. Schilling, I. Schwartz, and S. Knecht, “Parahydrogen-Polarized Fumarate for Preclinical in Vivo Metabolic Magnetic Resonance Imaging,” *J. Am. Chem. Soc.* **145**, 5960–5969 (2023).
- ¹⁵H. Jóhannesson, O. Axelsson, and M. Karlsson, “Transfer of Para-Hydrogen Spin Order into Polarization by Diabatic Field Cycling,” *C. R. Phys.* **5**, 315–324 (2004).
- ¹⁶A. Bornet, X. Ji, D. Mammoli, B. Vuichoud, J. Milani, G. Bodenhausen, and S. Jannin, “Long-Lived States of Magnetically Equivalent Spins Populated by Dissolution-DNP and Revealed by Enzymatic Reactions,” *Chem.- Eur. J.* **20**, 17113–17118 (2014).
- ¹⁷B. Ripka, J. Eills, H. Kouřilová, M. Leutzsch, M. H. Levitt, and K. M'unnemann, “Hyperpolarized fumarate via parahydrogen,” *Chem. Commun.* **54**, 12246–12249 (2018).
- ¹⁸K. Mouloudakis, S. Bodenstedt, M. Azagra, M. W. Mitchell, I. Marco-Rius, and M. C. D. Tayler, “Real-Time Polarimetry of Hyperpolarized ^{13}C Nuclear Spins Using an Atomic Magnetometer,” *J. Chem. Phys. Lett.* **14**, 1192–1197 (2023).
- ¹⁹B. A. Rodin, J. Eills, R. Picazo-Frutos, K. F. Sheberstov, D. Budker, and K. L. Ivanov, “Constant-Adiabaticity Ultralow Magnetic Field Manipulations of Parahydrogen-Induced Polarization: Application to an AA'X Spin System,” *Phys. Chem. Chem. Phys.* **23**, 7125–7134 (2021).
- ²⁰J. Eills, M. W. Mitchell, I. M. Rius, and M. C. D. Tayler, “Live Magnetic Observation of Parahydrogen Hyperpolarization Dynamics,” *Proc. Natl. Acad. Sci. U.S.A.* **121**, e2410209121 (2024).
- ²¹J. Eills, E. Cavallari, R. Kircher, G. Di Matteo, C. Carrera, L. Dagys, M. H. Levitt, K. L. Ivanov, S. Aime, F. Reineri, K. M'unnemann, D. Budker, G. Buntkowsky, and S. Knecht, “Singlet-contrast magnetic resonance imaging: Unlocking hyperpolarization with metabolism,” *Angew. Chem. Int. Ed.* **60**, 6791–6798 (2021).
- ²²M. Carravetta and M. H. Levitt, “Theory of Long-Lived Nuclear Spin States in Solution Nuclear Magnetic Resonance. I. Singlet States in Low Magnetic Field,” *J. Chem. Phys.* **122** (2005).
- ²³M. H. Levitt, “Demagnetization Field Effects in Two-Dimensional Solution NMR,” *Concepts Magn. Reson.* **8**, 77–103 (1996).
- ²⁴F. Wang, M. Ren, W. Sun, M. Guo, M. J. Sellars, R. L. Ahlefeldt, J. G. Bartholomew, J. Yao, S. Liu, and M. Zhong, “Nuclear Spins in a Solid Exceeding 10-Hour Coherence Times for Ultra-Long-Term Quantum Storage,” *PRX Quantum* **6** (2025).
- ²⁵D. A. Broadway, J. D. A. Wood, L. T. Hall, A. Stacey, M. Markham, D. A. Simpson, J.-P. Tetienne, and L. C. L. Hollenberg, “Anticrossing Spin Dynamics of Diamond Nitrogen-Vacancy Centers and All-Optical Low-Frequency Magnetometry,” *Phys. Rev. Appl.* **6** (2016).
- ²⁶V. E. Manucharyan, J. Koch, L. I. Glazman, and M. H. Devoret, “Fluxonium: Single Cooper-Pair Circuit Free of Charge Offsets,” *Science* **326**, 113–116 (2009).
- ²⁷F. Bao, H. Deng, D. Ding, R. Gao, X. Gao, C. Huang, X. Jiang, H.-S. Ku, Z. Li, X. Ma, X. Ni, J. Qin, Z. Song, H. Sun, C. Tang, T. Wang, F. Wu, T. Xia, W. Yu, F. Zhang, G. Zhang, X. Zhang, J. Zhou, X. Zhu, Y. Shi, J. Chen, H.-H. Zhao, and C. Deng, “Fluxonium: An Alternative Qubit Platform for High-Fidelity Operations,” *Phys. Rev. Lett.* **129** (2022).
- ²⁸K. L. Ivanov, A. N. Pravdítsev, A. V. Yurkovskaya, H.-M. Vieth, and R. Kaptein, “The Role of Level Anti-Crossings in Nuclear Spin Hyperpolarization,” *Prog. Nucl. Magn. Reson. Spectrosc.* **81**, 1–36 (2014).
- ²⁹L. Buljubasich, M. Franzoni, H. Spiess, and K. M'unnemann, “Level Anti-Crossings in ParaHydrogen Induced Polarization Experiments with Cs-Symmetric Molecules,” *J. Magn. Reson.* **219**, 33–40 (2012).
- ³⁰L. Dagys, M. C. Korzeczek, A. J. Parker, J. Eills, J. W. Blanchard, C. Bengs, M. H. Levitt, S. Knecht, I. Schwartz, and M. B. Plenio, “Robust Parahydrogen-Induced Polarization at High Concentrations,” *Sci. Adv.* **10** (2024).
- ³¹M. C. D. Tayler and S. Bodenstedt, “NMRduino: A Modular, Open-Source, Low-Field Magnetic Resonance Platform,” *J. Magn. Reson.* **362**, 107665 (2024).

³²S. Bodenstedt, M. W. Mitchell, and M. C. D. Tayler, “Fast-field-cycling Ultralow-field Nuclear Magnetic Relaxation Dispersion,” *Nat. Commun.* **12**, 4041 (2021).

³³C. Bengs and M. H. Levitt, “SpinDynamica: Symbolic and Numerical Magnetic Resonance in a Mathematica Environment,” *Magn. Reson. Chem.* **56**, 374–414 (2018).

V. METHODS

PHIP polarization of [1-¹³C]-fumarate

To produce hyperpolarized [1-¹³C]-fumarate, the precursor solution for all experiments was 125 mM acetylenedicarboxylic acid disodium salt (Merck), 125 mM sodium sulfite, and 3.5 mM ruthenium catalyst (pentamethyl cyclopentadienyl tris(acetonitrile) ruthenium(II) hexafluorophosphate) (Merck, CAS 99604-67-8) in ~99% D₂O, at pH 10-11. For each measurement, 600 μ L of the solution was loaded by pipette into a 5 mm screw-top NMR tube, and the tube was sealed. The screw top had two 1/16" (o.d.) PTFE capillaries passing through, acting as an inlet and an outlet for the hydrogen gas. The tube was pressurized to 5 bar with parahydrogen, and its lower end placed into a mineral oil bath for the solution to warm (115 °C, 10 s). While still in the hot bath, parahydrogen was flowed through the tubes and bubbled through the solution (5 bar for 60 s). Completion of the reaction was indicated by a pink/red color of the solution. The tube was then depressurized, cooled in a water bath, opened, and the solution was extracted through a PTFE capillary into a 1 mL syringe. The solution was then injected through a capillary tube into a 2 mL, 8-425 vial (Merck) located inside the shielded apparatus of Fig. 3; the delay between the end of the reaction and the start of field sweeps was 15 to 20 s.

Field control

For magnetic field control and shielding, a multi-layer MuMetal magnetic shield in a cylinder shape was used (Twinleaf model MS-1F, dimensions 30 cm length and 25 cm diameter). Inside the shield, a solenoid coil (7.5 mT/A, 15 mm diameter) was positioned parallel to the cylinder axis. The B_z magnetic field was generated using a 12-bit digital-to-analog converter (DAC) integrated circuit (MCP4822, MicroChip Technology Inc.) whose output was connected to the solenoid and a series shunt resistor. The DAC was digitally interfaced with a microcontroller, provided as part of the “NMRduino” open-source magnetic resonance platform³¹.

The solenoid field strength was calibrated at each DAC output voltage from the measured ¹H precession frequen-

cies of distilled water via a pulse-acquire experiment, following ex-situ prepolarization of the sample at 2 T³¹.

Optical magnetometry

The OPM used for detection comprised a cube-shaped alkali-metal vapor cell as its sensitive element (5 × 5 × 8 mm³), inside which ⁸⁷Rb and N₂ buffer gas was contained and heated to 150 °C. A D₁-resonant (795 nm), circularly polarized light beam was passed through one of the cube faces to optically pump the atomic spin polarization of the vapor. A second, off-resonance beam was passed through one of the other faces, and out of the opposing side, to probe the atomic polarization via optical rotation. The noise floor in the 10 to 100 Hz frequency range was 12 fT/√Hz.

The remaining cube face was placed against the exterior of the solenoid coil, near to the sample vial, with a standoff distance of 5-6 mm between the vapor cell and the vial. Further details of the magnetometer can be found in past work³².

Data acquisition and processing

The rotation angle of the OPM probe beam was detected at a balanced polarimeter (Thorlabs PDB210A), which produced a differential output voltage linearly proportional to the z - and x -axis magnetic field amplitude. The voltage was digitized by a second “NMRduino”³¹ device (16 bit, ~150 μ V/bit, 1–5 kHz sampling rate), and streamed to a computer via USB and displayed on-screen in real time after digital low-pass filtering. The raw signal data were also stored in a file on the computer for future retrieval, processing and plotting. Data processing operations to generate the plots shown in Fig. 3 involved simple operations in Mathematica (Wolfram Inc.) including: (i) a 25 Hz second-order low-pass Hamming or moving-average filter to suppress 50 Hz mains-electricity noise, which was the dominant noise source of the magnetometer, and (ii) Fourier transformation. A record of these operations is contained in the Supporting Dataset.

Simulations

Simulations were carried out using the SpinDynamica packages for Mathematica.³³ All simulations involved three spins, two ¹H and one ¹³C, and the interactions considered were the Zeeman interaction between the spins, the applied magnetic fields (in x , y , or z) and the spin-spin J -couplings (untruncated couplings in all cases). Chemical shifts were omitted because at such low fields these terms are negligible.